Hierarchical Self-Assembly and Optical Disassembly for Controlled Switching of Magnetoferritin Nanoparticle Magnetism

Mauri A. Kostiainen,[†,‡,*] Pierpaolo Ceci,[§] Manuela Fornara,[§] Panu Hiekkataipale,[‡] Oksana Kasyutich,[⊥] Roeland J. M. Nolte,[†] Jeroen J. L. M. Cornelissen,[¶] Ryan D. Desautels,[#] and Johan van Lierop[#,*]

[†]Institute for Molecules and Materials, Radboud University Nijmegen, Heyendaalseweg 135, 6525 AJ, Nijmegen, The Netherlands, [‡]Molecular Materials, Department of Applied Physics, Aalto University, P.O. Box 15100, FI-00076 Aalto, Espoo, Finland, [§]Department of Biochemical Sciences, CNR Institute of Molecular Biology and Pathology, "Sapienza", University of Rome, P.le Aldo Moro 5, 00185 Rome, Italy, [⊥]Engineering Faculty, University of Bristol, Woodland Road, Bristol, BS8 1UB, U.K., [¶]Laboratory for Biomolecular Nanotechnology, MESA+Institute for Nanotechnology, University of Twente, P.O. Box 217, 7500 AE Enschede, The Netherlands, and [#]Department of Physics and Astronomy, University of Manitoba, Winnipeg, Manitoba, R3T 2N2, Canada

ABSTRACT Protein cages such as ferritin and viral capsids are interesting building blocks for nanotechnology due to their monodisperse structure and ability to encapsulate various functional moieties. Here we show that recombinant ferritin protein cages encapsulating Fe_3O_4–γ-Fe_2O_3 iron oxide (magnetoferritin) nanoparticles and photodegradable Newkome-type dendrons self-assemble into micrometer-sized complexes with a face-centered-cubic (fcc) superstructure and a lattice constant of 13.1 nm. The magnetic properties of the magnetoferritin particles are affected directly by the hierarchical organization. Magnetoferritin nanoparticles dispersed in water exhibit typical magnetism of single domain noninteracting nanoparticles; however, the same nanoparticles organized into fcc superstructures show clearly the effects of the altered magnetostatic (*e.g.*, dipole–dipole) interactions by exhibiting, for example, different hysteresis of the field-dependent magnetization. The magnetoferritin–dendron assemblies can be efficiently disassembled by a short optical stimulus resulting in release of free magnetoferritin particles. After the triggered release the nanomagnetic properties of the pristine magnetoferritin nanoparticles are regained.

KEYWORDS: dendrimers and dendrons · ferritin · nanoparticle · self-assembly · magnetism

Electrostatic self-assembly of nanoscale-sized particles has emerged as a powerful approach for the construction of various hierarchical nanoparticle superstructures.[1−3] Not only are nanoparticles and their higher-order assemblies important for optics, drug delivery, and sensing applications, but they are also interesting from a fundamental point of view in understanding and developing new self-assembled structures and materials.[4−11] Protein cages constitute an interesting class of nanoparticles that allow the integration of biological and synthetic building blocks in a well-defined manner.[12−15] Various protein cages, such as virus capsids and iron-storage proteins, can be used for example as precisely defined scaffolds for the preparation of new materials, as hollow shells to encapsulate inorganic materials, or as multivalent ligand displays for targeting and delivery applications.[16−23] A key advantage of the protein cages is the possibility to assemble them into higher-order hierarchical arrays, which in principle offers the potential to direct the assembly and organization of various materials that can be encapsulated inside the cage.[24−28]

We are interested in the ferritin cage, which consists of 24 protein subunits that self-assemble into a hollow globular shell with 432 symmetry.[29] The outer and inner diameters of the ferritin cage are 12 and 8 nm, respectively. Ferritin cages have been arranged previously into ordered one-, two- and three-dimensional arrays using various assembly techniques.[26,30−34] In 1992 Meldrum *et al.* were the first to demonstrate a biomimetic synthesis of artificial Fe_3O_4–γ-Fe_2O_3 iron oxide nanoparticles inside the ferritin cage (magnetoferritin).[35] Later in-depth characterization of their magnetic properties revealed no magnetic hysteresis in the field-dependent magnetization at temperatures down to 30 K (the blocking temperature, T_B) in accord with the superparamagnetic behavior of single-domain particles that had magnetizations between 10 000 and 13 000 Bohr magnetons (μ_B).[36] In addition, the magnetoferritin nanoparticles had an uniaxial anisotropy energy (K, the amount of thermal- or magnetic-field-energy required to cause

* Address correspondence to mauri.kostiainen@aalto.fi, johan@physics.umanitoba.ca.

Received for review April 29, 2011 and accepted July 8, 2011.

Published online July 15, 2011
10.1021/nn201571y

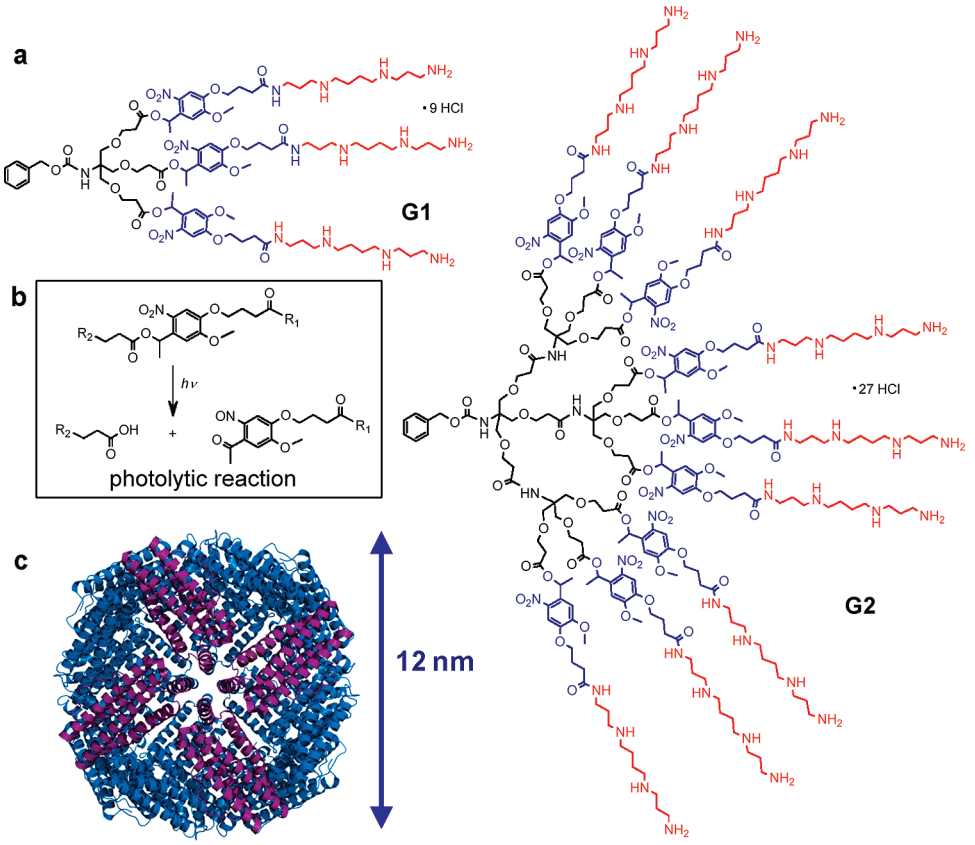

Figure 1. Building blocks for self-assembly: (a) optically degradable dendrons used to complex RMPs; (b) schematic representation of the photolytic reaction; (c) structure of the ferritin cage from *Pyrococcus furiosus* viewed along the 4-fold symmetry axis.

a 180° flip of the single-domain particle's magnetization) of $\sim 10^{-20}$ J.

Previous studies of three-dimensional magnetostatic interactions among nanoparticles have been limited to a few layers of well-crystallized layers of nanoparticles[37] or mixed hexagonally close-packed (h.c.p.) and fcc orientations of nanoparticles.[38] Only recently the preparation of macroscopic (face side lengths of several hundred micrometers) crystalline assemblies of magnetoferritin nanoparticles has been presented.[33,34] These crystals with fcc configuration revealed markedly different magnetism when compared to a disordered ensemble of magnetoferritin nanoparticles. The nanoparticle-based crystal presented ferromagnet-like magnetism up to 400 K, whereas, without the benefit of the unique organization of interparticle interactions present in the crystal, the uncrystallized nanoparticles were superparamagnetic, that is, with a coercivity $H_c = 0$ at 400 K. The magnetoferritin nanoparticles themselves presented typical nanomagnetism; for example, the largest $H_c(T)$ was at the lowest temperatures because of the field required to rotate the single domain of the particle and overcome the energy barrier describing the moment reversal ($\Delta E = KV$ where V is the particle's volume).[39]

While the 3D nanoparticle crystal magnetism is fascinating from a fundamental physics viewpoint, the ability to switch structure hierarchies between two length scales, that is, micro- (crystal) and nano- (single particle) scales by applying external stimuli and hence between two physical behaviors of matter, is a very significant and attractive advantage of this system from an applications point of view.[40,41] This approach could for example offer the possibility of using crystals of nanoparticles that are drug coated and ferromagnetic, providing an optimal external driving field for controlled magnet field targeted drug delivery purposes. Disassembly into their usual superparamagnetic configuration would enable simultaneous magnetic hyperthermia and controlled drug release.[42]

To create self-assembled nanoparticle crystals that can be disassembled to recover the intrinsic magnetism of the component, our approach has been to use photolabile dendrons to promote interparticle interactions (Figure 1).[43] Nanoparticles in our study are constituted of recombinant magnetoferritin particles (RMPs)—iron oxide encapsulated with the ferritin protein cage from hyperthermophile *Pyrococcus furiosus*.[44] The dendrons are surface functionalized with spermine units, which carry a positive charge (pK_a amines > 8) and can therefore form electrostatic complexes with

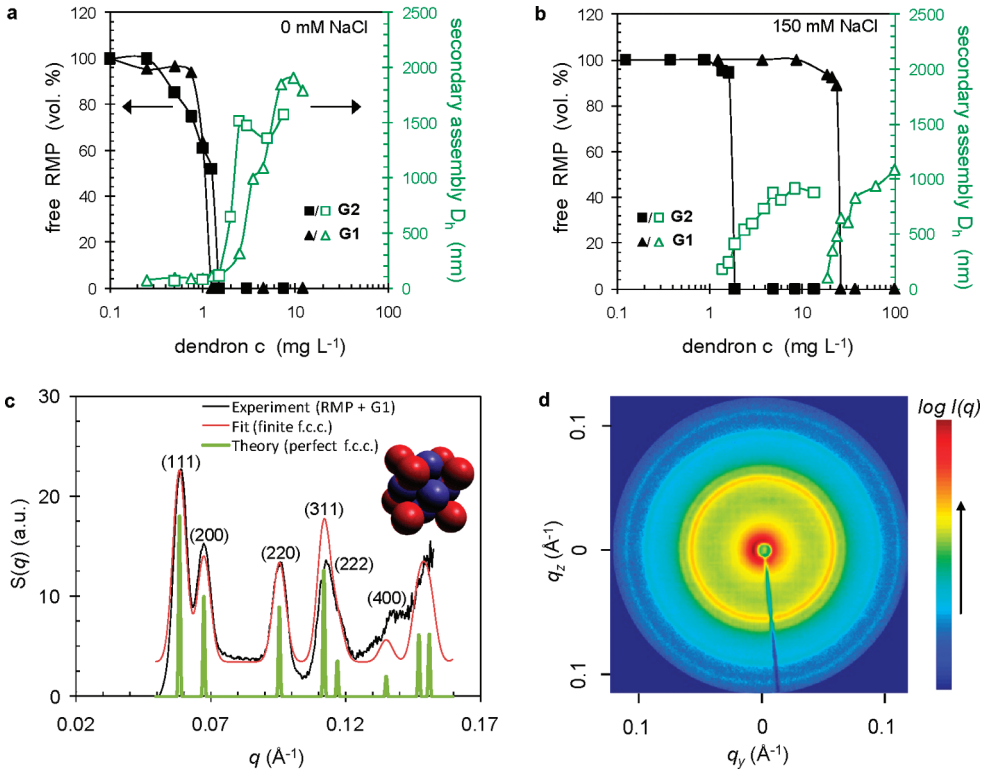

Figure 2. Self-assembly of RMP−dendron complexes. DLS results for the titration of a RMP solution (25 mg L^{-1}) with G1 and G2 in the presence of 0 (a) and 150 mM (b) NaCl indicate that the RMP−G1 complex formation is sensitive to the increase in ionic strength. Figures show a decrease in the volume averaged scattering intensity of the free RMPs (full symbols, primary axis) and formation of larger secondary assemblies (open green symbols, secondary axis). (c) Integrated SAXS patterns from RMP solution (10 mg mL^{-1}) complexed with G1 (8 mg mL^{-1}) (solid black line) matches well with a theoretical fcc structure. An illustration of fcc packed spheres is presented in the inset. (d) 2D SAXS image of RMP−G1 complex presented in panel c.

the negatively charged RMPs that have an isoelectric point (PI) of ~4.5 (Figure 1).[45] The spermine surface groups are attached to the dendritic scaffold through photolabile *o*-nitrobenzyl linkers,[46] which can be easily cleaved by a short exposure to UV light[47,48] This methodology allows a controlled breakdown of the multivalent surface and release of the covalently attached spermine groups. The resulting individual spermine groups have only a weak affinity toward RMPs, permitting the complexes to disassemble. Importantly, this optical triggering allows a spatially and temporally controlled release event.

TABLE 1. RMP Binding Data Extracted from the DLS Experiments at Different NaCl Concentrations, Showing the Amount of Dendron Needed to Assemble 50% of the Free RMPs As Observed by the Volume-Averaged Scattering Intensity

compound	[NaCl] [mM]	nominal charge	c_{50} [mg L^{-1}] [a]	cm_{50} [μM]	ce_{50}
G1	0	+9	1.12	0.600	5.40
G2	0	+27	1.39	0.247	6.68
G1	150	+9	25.14	13.457	121.11
G2	150	+27	1.76	0.313	8.46

[a] Higher c_{50} values represent a lower tendency to form complexes with RMPs.

RESULTS AND DISCUSSION

Initially, the formation of RMP−dendron complexes was investigated at two different ionic strengths (0 and 150 mM NaCl) with dynamic light scattering (DLS). A RMP solution (25 mg L^{-1}) was titrated with small aliquots of **G1** and **G2** and the formation of the complexes was followed by monitoring the increase in hydrodynamic diameter D_h (Figure 2 and Supporting Information, Figure S1). The expected diameter of free RMP is 12 nm, which can also be observed by DLS. When the concentration of **G1** or **G2** is increased, the peak corresponding to the free RMPs is decreased and gradually disappears completely. At the same time, a large secondary assembly starts to form, which grows in size with increasing dendron concentration. The DLS data can be plotted as shown in Figure 2a,b to highlight the decrease of the free RMP volume fraction (volume %, primary *y*-axis) and the accompanying increase in the secondary assembly diameter (D_h, secondary *y*-axis). The efficiency of **G1** and **G2** to complex RMPs can be defined with a c_{50} value, which represents the concentration of polymer needed to assemble 50% of the free RMPs, as observed by volume-averaged scattering intensity (Table 1). The c_{50} values can also be presented as the cm_{50}, which give the molar concentration, or normalized to the nominal charge concentration to give the ce_{50} values.

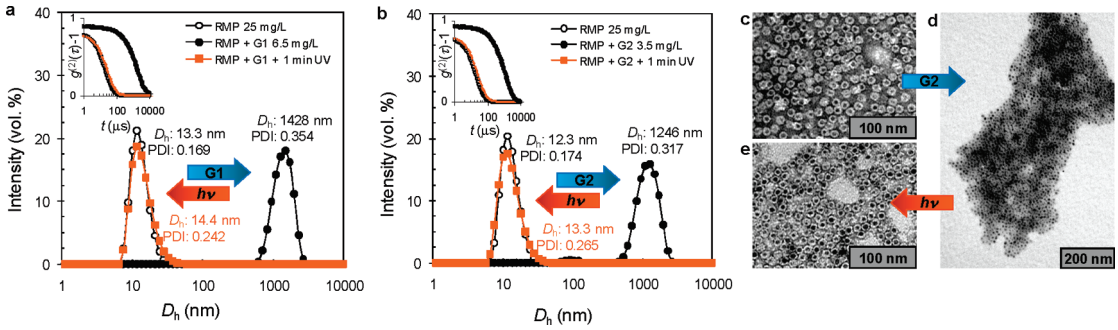

Figure 3. Disassembly of the RMP−dendron complex. DLS traces of (a) RMP−G1 and (b) RMP−G2 complexes before and after UV irradiation showing that the large assemblies can be clearly formed and subsequently disassembled. Insets: corresponding second-order correlation functions. (c−e) Negatively stained (uranyl acetate) TEM micrographs of free RMPs (c), RMP−G2 complex (d), and a RMP−G2 complex after 1 min UV exposure (e) showing free and intact RMPs again.

Figure 2 indicates that the assembly of RMP−dendron complexes is highly sensitive to the dendritic generation and NaCl concentration. In the absence of NaCl, both **G1** and **G2** complex the RMPs efficiently in similar manner (c_{50} = 1.1 and 1.4 mg L^{-1} respectively, Figure 2a and Table 1). Also the diameter of the secondary assembly increases in concert with increasing dendron concentration although the maximum hydrodynamic diameter is observed to set between 1.5−2 μm. We argue that the formation of the secondary assembly is largely driven by electrostatic attraction between the polyelectrolyte dendron and charged RMP surface. A possible reason for the observed maximum is that while the complexes are formed, strong electrostatic repulsion is introduced because polyelectrolytes of similar charge are brought in close proximity. Consequently at higher dendron concentrations the attractive electrostatic interactions are opposed efficiently enough to limit the assembly size.[49−51] Time course of the assembly process is rapid and the assemblies form approximately in 10 min (Supporting Information, Figures S2 and S3). When the NaCl concentration is increased to 150 mM, the formation of RMP−dendron complexes becomes less pronounced due to the fact that the increased ionic strength can efficiently screen the attractive electrostatic interactions (Figure 2b). **G1** loses much of complexing affinity and as a result the c_{50} value increases to 25.1 mg L^{-1}. Conversely, the complexing affinity of **G2** is only a little affected by the increase in ionic strength (c_{50} = 1.8 mg L^{-1}), probably due to ligand sacrifice that helps to protect the binding site.[52] The assembly size increases in a manner similar to that as in the absence of salt, although the maximum diameter for the assemblies is reached at approximately 1 μm.

Small angle X-ray scattering (SAXS) was used to characterize the structural configuration of the RMP−dendron complexes. Integrated and background corrected SAXS curves in Figure 2c show typical scattering obtained from a RMP solution complexed with **G1** (see Supporting Information, Figure S4 for raw SAXS data). The two-dimensional (Figure 2d) scattering pattern shows clear first-order SAXS reflection from the (*hkl*) = (111) plane at magnitude of the scattering vector q^* = 0.588 nm^{-1}. Multiple higher-order reflections at 0.660, 0.956, 1.126, 1.179, and 1.352 nm^{-1} are also readily observed and correspond to reflections from the (200), (220), (311), (222), and (400) planes, respectively. The peak position ratios are $q^n/q^* \approx \sqrt{1}:\sqrt{(^4/_3)}:\sqrt{(^8/_3)}:\sqrt{(^{11}/_3)}:\sqrt{2}$ and $\sqrt{(^{16}/_3)}$, corresponding to a fcc structure (depicted in the Figure 2 inset) with a lattice parameter a of 18.5 nm, as calculated from the distance between lattice planes d ($a = 2d/\sqrt{(^4/_3)}$). The relative peak heights and positions match well with theoretical calculations of such structures. Estimation with the Scherrer formula indicated that the single-crystal domain size is at least 0.5 μm. The average center-to-center interparticle distance can be determined from the lattice parameter as $a/\sqrt{2}$, which gives a measured distance of 13.1 nm. The observed interparticle distance corresponds clearly to the 12 nm diameter of the native ferritin cage. On the other hand, SAXS results on the free RMPs in a uncrystallized configuration did not show a distinct scattering pattern, but rather a dampening oscillation of scattering intensity, as expected for free spherical particles in solution. It is interesting to note that the electrostatic RMP−dendron complexes also adopt fcc packing similar to the pure magnetoferritin crystals,[34] indicating that this method is indeed viable to deliver ordered 3D crystals through self-assembly.

Disassembly of the complexes was studied initially with DLS (Figure 3). Free RMPs were first fully complexed with the dendrons and then exposed to a short period of UV irradiation. Figure 3a,b shows a typical assembly/disassembly cycle. The measured D_h for free RMPs lies approximately between 12−13 nm (polydispersity indices, PDI ≈ 0.17). Ferritins are known to exhibit slightly elevated PDI values at low ionic strength medium.[53] Upon the addition of **G1** or **G2** the complexes were formed and the D_h was increased to >1.2 μm. The samples were then irradiated with UV light for 1 min. The UV irradiation induced the disassembly of the complexes, and the original

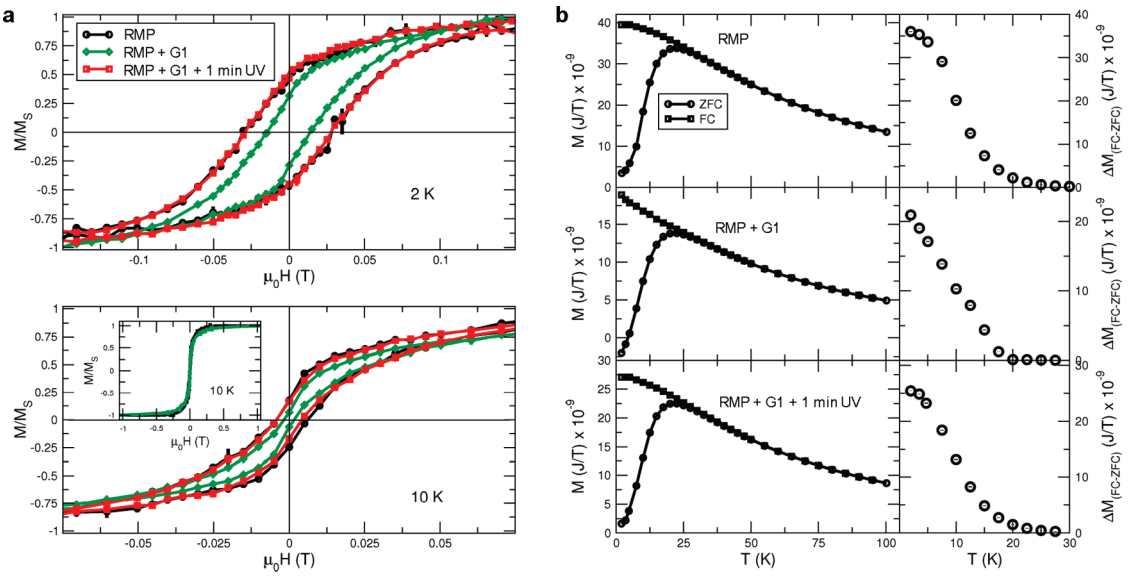

Figure 4. Comparison of the magnetic properties between disordered and fcc arranged RMP-G1 complexes. (a) Hysteresis loops at 2 K (top) and 10 K (bottom) for the free RMPs, the RMP−G1 complexes with fcc configuration, and the RMP−G1 complexes disassembled with 60 s of UV irradiation (free RMPs). The inset in the bottom figure shows the full ±1 T loop taken at 10 K for all three systems identifying clear magnetic saturation with fields greater than ±0.5 T. The solid lines are a guide to the eye. (b) Temperature dependence of the low field magnetization (M) when the systems were zero-field-cooled (ZFC) and field-cooled (FC) from 300 K using a 0.01 T measuring field. The plots show results for (from top to bottom): free RMPs, RMP−G1 complex with fcc configuration, and the RMP−G1 complex after 60 s of UV exposure. At right are the respective difference plots of the FC and ZFC magnetizations as a function of temperature showing the different temperature dependencies of the system's anisotropies.

size-distribution profile corresponding to free RMPs was regained, indicating clearly that the photolytic reaction had taken place. To complement the DLS results and to visualize the structural morphology of the free RMPs and their assemblies, transmission electron microscopy (TEM) images were acquired (Figure 3c,d). Figure 3c shows a typical negatively stained image of free RMPs with the electron dense iron-oxide core surrounded by the ferritin protein shell. The average diameter of the RMPs was 12.4 ± 0.7 nm. Samples deposited from a solution containing RMP−**G2** complexes showed the presence of large 3-dimensional assemblies with diameters of several hundreds of nanometre (see Supporting Information, Figure S5 for images of RMP−**G1** complexes). UV exposure efficiently degraded the complexes, which were no longer observed on the TEM grids, and only free RMPs with an average diameter of 12.5 ± 0.6 nm were observed.

Magnetometry and susceptometry experiments with a superconducting quantum interference device (SQUID) revealed clear differences in the nanomagnetism of the freely dispersed (uncrystallized) RMPs, and the RMP assemblies formed with the **G1** dendron (Figure 4). As shown in Figure 4a, the free RMPs exhibited typical single-phased magnetization (M) *versus* field (μ_0H) dependence, with a saturation field (M_s) and largest measured coercivity (H_c) at the lowest temperatures, with H_c decreasing with warming. Here, H_c demarks the field required to reverse the magnetization direction of the RMPs. The impact of the coordinated interparticle interactions (*e.g.*, dipole−dipole) in the fcc RMP−**G1** complexes was readily observed even at 2 K, when compared to the random interparticle interactions in the free RMPs. A significantly lower H_c was observed, indicating that the ordered interactions have effectively reduced the magnetic anisotropy (*K*) of the system (where the energy necessary to reorient the magnetization of a single-domain particle is described by *KV*, where *V* is the particle's volume). This collective behavior has been predicted recently *via* Monte Carlo[54] and Landau−Lifshitz−Gilbert dynamic[55] simulations of single-spin systems in lattices. Additionally, it has been demonstrated experimentally[37,56] that the interacting surface spins provide a surface anisotropy in a magnetite nanoparticle system which is predominant at low temperatures (2 K). Hence the effective magnetic behavior at this temperature is dominated by the surface spins, which manifests as a monotonic M *versus* μ_0H loop.

At slightly higher temperatures (*e.g.*, 10 K), not only is H_c still weaker in the RMP−**G1** complex in comparison to the free RMPs, but the M *versus* μ_0H behavior is no longer single-phased. This biconcave-shaped hysteresis curve is indicative of two different magnetic anisotropies being present. As the two anisotropies required different Fe spin populations to occur, we attribute this magnetism to the possible counteralignment of core and surface Fe spins. The usual M *versus* μ_0H trends of the free RMPs are due to the surface Fe spins being disordered, much like a spin-glass.

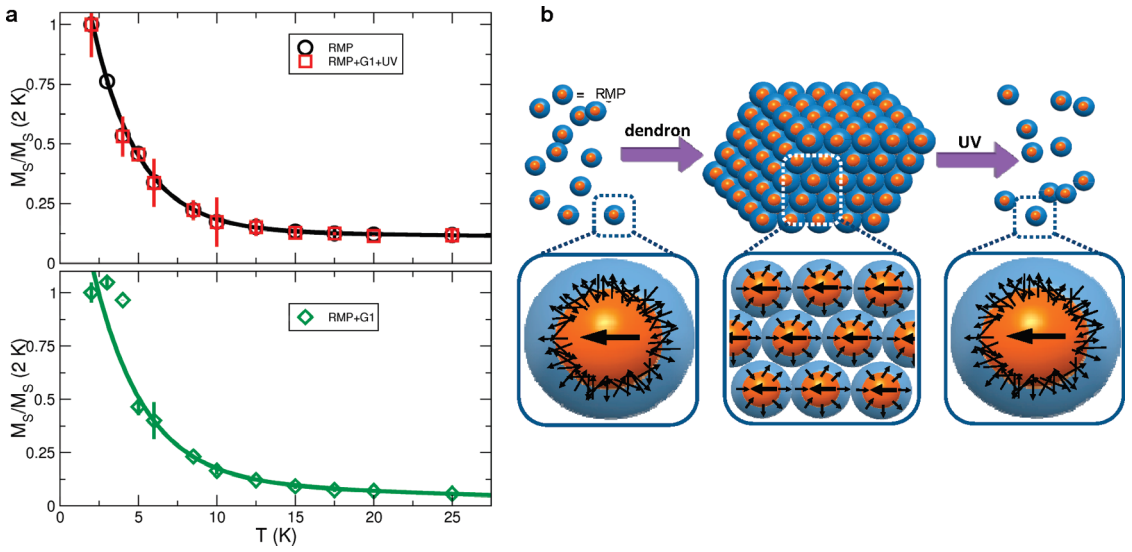

Figure 5. Spin alignment at low temperatures. (a) Temperature dependence of the saturation magnetization (M_s) for the free RMPs and UV disassembled RMP−G1 complex (top) and the RMP−G1 complex with fcc configuration (bottom). The fit (solid line) in the top panel is described in the text and overlaid with the data points in the bottom panel to emphasize the difference below 5 K. (b) Strategy for the assembly and optically triggered disassembly of RMP−dendron complexes and a schematic representation of the surface/core-spin alignment in the presence of a magnetic field.

Since the nanomagnetism of a system is acutely dependent on its structure, an important test of the UV disassembly is whether exactly the same nanomagnetism is observed in the free RMPs and RMP−**G1** complexes disassembled with UV-light. Indeed, that is the case, since virtually identical M *versus* μ_0H curves are observed at 2 and 10 K as shown in Figure 4a. The 60 s UV irradiation of the RMP−**G1** complexes "resets" the structure and magnetism to that of the free RMPs.

In Figure 4b we show the zero-field-cooled (ZFC) and field-cooled (FC) magnetization's (M) temperature dependence in a low field (0.01 T) for the three systems. When the RMPs undergo a ZFC process at low temperature, the magnetization of a single-domain particle will be static and fixed along its easy axis direction, which is set by the magnetocrystalline anisotropy. Furthermore, the configurational disorder of the nanoparticle dispersion, as is the case for the free RMPs, will ensure that the average system magnetization is smallest (if not zero). Application of a small measuring field will permit the resultant magnetization of the component of RMP's magnetization along the field direction, so that a nonzero M is determined. With warming, the single-domain moment will oscillate around its easy axis direction and M will increase as the magnetization of the particles can respond to the applied field. When the nanoparticle system reaches the temperature where nanoparticle moments begin to undergo superparamagnetic spin-flips during the time-window of the measurements (essentially DC for a M *vs T* scan), the maximal M is measured. With further warming above the blocking temperature T_B that is set by *K* and *V*, the measured time-averaged magnetization decreases, and this is mirrored in the gradual decrease of M. This ZFC behavior of the magnetization is reflected in all RMP−based systems. However, cooling the nanoparticle systems in a field (M_{FC} in Figure 4b) reveals clearer differences between the free RMPs and RMP−**G1** complexes, and further demonstrates that the UV disassembly of the fcc arranged RMP−**G1** complex is complete. Upon cooling from temperatures significantly above T_B there is a measured divergence between the zero field (M_{ZFC}) and M_{FC} at T_B (~25 K, in good agreement with similar magnetoferritin nanoparticle systems) since the applied field keeps the RMP's magnetization aligned with the field. By this usual phenomenological assessment, T_B is essentially unchanged; however, at the lowest temperatures the bare (and UV disassembled) RMP systems M_{FC} becomes constant; all possible moments (nanoparticle and atomic) are aligned with the applied field. By contrast, M_{FC} for the RMP−**G1** complex continues to increase monotonically even to the lowest temperature of 2 K. This very different nanomagnetism, driven by the unique dipole−dipole magnetostatic interactions, is revealed clearly by the temperature dependence of ΔM (=M_{FC} − M_{ZFC})(*T*), which reflects the different temperature dependence of the system's magnetic anisotropy.

The temperature dependence of M_s establishes further differences between the nanomagnetism of the free RMPs and RMP−**G1** complexes due to the differences in magnetostatic interparticle interactions. For example, the free RMPs show typical core/surface nanomagnetism characteristics, with the exponential-like $M_s(T)$ between 2 and 10 K from surface spins that "thaw" with warming and become paramagnetic or undergo rapid transverse relaxation resulting in a

time-averaged reduction of their magnetization. Furthermore, the higher temperature $M_s(T)$ is constant since the core of the nanoparticle is ordered magnetically; that is, the Curie temperature for the RMP maghemite/magnetite complex is around 850 K (ignoring finite-size effects that typically lower the Curie temperature). To gain an estimate of the spin-freezing temperatures, experimental data in Figure 5a is fitted with a solid line to lower temperature $M_s(T) = A \exp(-T/T_f)$, where T_f is the spin-freezing temperature and A describes a phenomenological constant that scales with the relative amount of frozen surface moments.[57] The fit identified a $T_f = 3.95 \pm 0.05$ K, which is in good agreement with previous studies of surface spin freezing in iron-oxide nanoparticles.[39] By contrast, the low temperature $M_s(T)$ of the RMP–**G1** complex is quite different, with $M_s(T)$ constant between 2 and 5 K followed by a sudden decrease above 5 K where presumably the surface spins are thawing. This behavior indicates that the surface spins are polarized and experienced a coherent alignment as opposed to the disordered surface spin configuration of the individual RMPs and therefore are not disordered in a spin-glass-like configuration as is the case for the free RMPs. Between 5 and 15 K, $M_s(T)$ decreases gradually in a manner similar to the free RMPs since the thermal energy has overcome the unique dipole–dipole interaction energy in the crystal system. The nanomagnetism between 2 and 5 K combined with the M *versus* μ_0H and FC–ZFC behavior described above leads us to postulate the moment configurations shown schematically in Figure 5b.

CONCLUSIONS

Our findings demonstrate that biohybrid magnetoferritin particles can be assembled into micrometer-sized crystals with fcc nanoparticle configuration by using multivalent dendrons that interact electrostatically with the particles. The assembly process can be reversed by a short optical stimulus that degrades the dendrons and consequently destroys the attractive interactions between the RMPs. This *in situ* induced switch presents an opportunity to investigate the interplay between the micro- (3D ordered, interacting) state and nano- (single particle, noninteracting) state. Importantly, we have established clear experimental evidence of the differences in the nanomagnetism of the free and fcc packed RMPs. One of the major differences was a significantly smaller magnetic field required to rotate the magnetization of the nanoparticle crystals. The ability to tune magnetic properties of nanoparticles by assembling them into ordered superstructures and to reverse the assembly process by external stimuli is foreseen to facilitate development of new practical applications.

EXPERIMENTAL SECTION

The synthesis of dendrons **G1** and **G2** and the preparation of RMPs are reported elsewhere.[44,58,59]

Dynamic light scattering experiments were carried out with a Zetasizer Nano S from Malvern Instruments at 25 °C. Results are the average of at least five measurements. All RMP samples were prepared in filtered MQ water (0 or 150 mM NaCl). The RMP solution (0.4 mL, 25 mg L^{-1}) was titrated with an aqueous dendron solution (0.001–10 mg mL^{-1} depending on the dendron and titration). The added dendron solution did not exceed 5% of the total volume, therefore no corrections were made for sample dilution. After each titrant addition, the samples were thoroughly mixed and allowed to equilibrate for 2 min.

Transmission electron microscopy micrographs were recorded on a JEOL JEM-1010 instrument. Samples were prepared on Formvar carbon-coated copper grids (Electron Microscopy Sciences) by placing on the grid a 5 μL drop of a solution containing a mixture of RMP (25 mg L^{-1}) and the dendron (1–10 mg L^{-1}). The sample drop was left standing for 1 min after which time the excess buffer was blotted away with filter paper. Samples were negatively stained by applying 5 μL of stain (1% uranyl acetate in Milli-Q water) onto the grid and removing the excess stain with filter paper after 15 s. The samples were dried under air flow for 5 min before imaging.

Small angle X-ray measurements were obtained as follows: RMP–dendron complexes were prepared by slowly mixing together 20 μL of RMP solution (10 mg mL^{-1}) and 3 μL of dendron solution (10 mg mL^{-1}). The samples were centrifuged at 10000*g* for 5 min after which the supernatant was discarded and the complexes resuspended in 10 μL of Milli-Q water. The samples were sealed in a metal holder between two Kapton films to yield a sample with a thickness of approximately 0.9 mm. The structural periodicities were measured by using a rotating anode Bruker Microstar microfocus X-ray source (Cu Kα radiation, $\lambda = 1.54$ Å) with Montel collimating optics. The beam was further collimated with four sets of slits (JJ X-ray), resulting in a beam of approximately 1 × 1 mm at the sample position. The distance between the sample and the Hi-Star 2D area detector (Bruker) was 1.59 m. One-dimensional SAXS data were obtained by azimuthally averaging the 2D scattering data. The magnitude of the scattering vector is given by $q = (4\pi/\lambda) \sin\theta$, where 2θ is the scattering angle.

Superconducting quantum interference device magnetometry/susceptometry measurements were performed in a Quantum Design Magnetic Properties Measurement System (MPMS). Magnetic shielding with field profiling about the sample position and field canceling with trim coils were used to ensure stray fields were nullified during zero-field cooling measurements. Aliquots of the RMP samples were pipetted into polycarbonate capsules and mounted into a holder using the reciprocating sample option (RSO) of the MPMS. Samples were quenched from room temperature to 250 K to ensure that the sample was frozen before the air was pumped out of the sample chamber and introduced to the He exchange gas temperature controlled measuring environment. The diamagnetic background contribution from the capsule, holder, and dendron complex to the high-field magnetization was characterized and subtracted from the raw data.

Acknowledgment. This work was supported by The Netherlands Organization for Scientific Research, European Research Council the Royal Netherlands Academy of Sciences, the Natural Sciences and Engineering Research Council of Canada, and the Canada Foundation for Innovation. M.K. thanks the Academy of

Finland, Instrumentarium Science Foundation, and the Alfred Kordelin Foundation for their support.

Supporting Information Available: Additional DLS, SAXS, and TEM data. This material is available free of charge *via* the Internet at http://pubs.acs.org.

REFERENCES AND NOTES

1. Kalsin, A. M.; Fialkowski, M.; Paszewski, M.; Smoukov, S. K.; Bishop, K. J. M.; Grzybowski, B. A. Electrostatic Self-Assembly of Binary Nanoparticle Crystals with a Diamond-like Lattice. *Science* **2006**, *312*, 420–424.
2. Leunissen, M. E.; Christova, C. G.; Hynninen, A.-P.; Royall, C. P.; Campbell, A. I.; Imhof, A.; Dijkstra, M.; van Roij, R.; van Blaaderen, A. Ionic Colloidal Crystals of Oppositely Charged Particles. *Nature* **2005**, *437*, 235–240.
3. Mann, S. Self-Assembly and Transformation of Hybrid Nano-objects and Nanostructures under Equilibrium and Non-equilibrium Conditions. *Nat. Mater.* **2009**, *8*, 781–792.
4. Jiang, P.; Bertone, J. F.; Hwang, K. S.; Colvin, V. L. Single-Crystal Colloidal Multilayers of Controlled Thickness. *Chem. Mater.* **1999**, *11*, 2132–2140.
5. Vlasov, Y. A.; Bo, X.-Z.; Sturm, J. C.; Norris, D. J. On-Chip Natural Assembly of Silicon Photonic Bandgap Crystals. *Nature* **2001**, *414*, 289–293.
6. De, M.; Rana, S.; Akpinar, H.; Miranda, O. R.; Arvizo, R. R.; Bunz, U. H. F.; Rotello, V. M. Sensing of Proteins in Human Serum Using Conjugates of Nanoparticles and Green Fluorescent Protein. *Nat. Chem.* **2009**, *1*, 461–465.
7. Holtz, J. H.; Asher, S. A. Polymerized Colloidal Crystal Hydrogel Films as Intelligent Chemical Sensing Materials. *Nature* **1997**, *389*, 829–832.
8. Elghanian, R.; Storhoff, J. J.; Mucic, R. C.; Letsinger, R. L.; Mirkin, C. A. Selective Colorimetric Detection of Polynucleotides Based on the Distance-Dependent Optical Properties of Gold Nanoparticles. *Science* **1997**, *277*, 1078–1081.
9. Lim, J.; Eggeman, A.; Lanni, F.; Tilton, R. D.; Majetich, S. A. Synthesis and Single-Particle Optical Detection of Low-Polydispersity Plasmonic-Superparamagnetic Nanoparticles. *Adv. Mater.* **2008**, *20*, 1721–1726.
10. Shevchenko, E. V.; Talapin, D. V.; Kotov, N. A.; O'Brien, S.; Murray, C. B. Structural Diversity in Binary Nanoparticle Superlattices. *Nature* **2006**, *439*, 55–59.
11. Srivastava, S.; Santos, A.; Critchley, K.; Kim, K.-S.; Podsiadlo, P.; Sun, K.; Lee, J.; Xu, C.; Lilly, G. D.; Glotzer, S. C.; *et al.* Light-Controlled Self-Assembly of Semiconductor Nanoparticles into Twisted Ribbons. *Science* **2010**, *327*, 1355–1359.
12. de la Escosura, A.; Nolte, R. J. M.; Cornelissen, J. J. L. M. Viruses and Protein Cages as Nanocontainers and Nanoreactors. *J. Mater. Chem.* **2009**, *19*, 2274–2278.
13. Lee, L. A.; Niu, Z.; Wang, Q. Viruses and Virus-like Protein Assemblies—Chemically Programmable Nanoscale Building Blocks. *Nano Res.* **2009**, *2*, 349–364.
14. Uchida, M.; Klem, M. T.; Allen, M.; Suci, P.; Flenniken, M.; Gillitzer, E.; Varpness, Z.; Liepold, L. O.; Young, M.; Douglas, T. Biological Containers: Protein Cages as Multifunctional Nanoplatforms. *Adv. Mater.* **2007**, *19*, 1025–1042.
15. Young, M.; Willits, D.; Uchida, M.; Douglas, T. Plant Viruses as Biotemplates for Materials and Their Use in Nanotechnology. *Annu. Rev. Phytopathol.* **2008**, *46*, 361–384.
16. Douglas, T.; Young, M. Host–Guest Encapsulation of Materials by Assembled Virus Protein Cages. *Nat.* **1998**, *393*, 152–155.
17. Tong, G. J.; Hsiao, S. C.; Carrico, Z. M.; Francis, M. B. Viral Capsid DNA Aptamer Conjugates as Multivalent Cell-Targeting Vehicles. *J. Am. Chem. Soc.* **2009**, *131*, 11174–11178.
18. Raja, K. S.; Wang, Q.; Finn, M. G. Icosahedral Virus Particles as Polyvalent Carbohydrate Display Platforms. *ChemBioChem* **2003**, *4*, 1348–1351.
19. Meldrum, F. C.; Wade, V. J.; Nimmo, D. L.; Heywood, B. R.; Mann, S. Synthesis of Inorganic Nanophase Materials in Supramolecular Protein Cages. *Nature* **1991**, *349*, 684–687.
20. Mann, S.; Archibald, D. D.; Didymus, J. M.; Douglas, T.; Heywood, B. R.; Meldrum, F. C.; Reeves, N. J. Crystallization at Inorganic–Organic Interfaces: Biominerals and Biomimetic Synthesis. *Science* **1993**, *261*, 1286–1292.
21. de la Escosura, A.; Verwegen, M.; Sikkema, F. D.; Comellas-Aragonès, M.; Kirilyuk, A.; Rasing, T.; Nolte, R. J. M.; Cornelissen, J. J. L. M. Viral Capsids as Templates for the Production of Monodisperse Prussian Blue Nanoparticles. *Chem. Commun.* **2008**, *44*, 1542–1544.
22. Nam, K. T.; Kim, D.-W.; Yoo, P. J.; Chiang, C.-Y.; Meethong, N.; Hammond, P. T.; Chiang, Y.-M.; Belcher, A. M. Virus-Enabled Synthesis and Assembly of Nanowires for Lithium Ion Battery Electrodes. *Science* **2006**, *312*, 885–888.
23. Yoo, P. J.; Nam, K. T.; Qi, J.; Lee, S.-K.; Park, J.; Belcher, A. M.; Hammond, P. T. Spontaneous Assembly of Viruses on Multilayered Polymer Surfaces. *Nat. Mater.* **2006**, *5*, 234–240.
24. Li, T.; Ye, B.; Niu, Z.; Thompson, P.; Seifert, S.; Lee, B.; Wang, Q. Closed-Packed Colloidal Assemblies from Icosahedral Plant Virus and Polymer. *Chem. Mater.* **2009**, *21*, 1046–1050.
25. Okuda, M.; Kobayashi, Y.; Suzuki, K.; Sonoda, K.; Kondoh, T.; Wagawa, A.; Kondo, A.; Yoshimura, H. Self-Organized Inorganic Nanoparticle Arrays on Protein Lattices. *Nano Lett.* **2005**, *5*, 991–993.
26. Yuan, Z.; Petsev, D. N.; Prevo, B. G.; Velev, O. D.; Atanassov, P. Two-Dimensional Nanoparticle Arrays Derived from Ferritin Monolayers. *Langmuir* **2007**, *23*, 5498–5504.
27. Kostiainen, M. A.; Hiekkataipale, P.; de la Torre, J. A.; Nolte, R. J. M.; Cornelissen, J. J. L. M. Electrostatic Self-Assembly of Virus Polymer Complexes. *J. Mater. Chem.* **2011**, *21*, 2112–2117.
28. Lambert, E. M.; Viravaidya, C.; Li, M.; Mann, S. Microemulsion-Mediated Self-Assembly and Silicification of Mesostructured Ferritin Nanocrystals. *Angew. Chem., Int. Ed.* **2010**, *49*, 4100–4103.
29. Theil, E. C. Ferritin: Structure, Gene Regulation, and Cellular Function in Animals, Plants, and Microorganisms. *Annu. Rev. Biochem.* **1987**, *56*, 289–315.
30. Kim, M. S.; Shin, K. M.; Kim, S. I.; Spinks, G. M.; Kim, S. J. Controlled Array of Ferritin in Tubular Nanostructure. *Macromol. Rapid Commun.* **2008**, *29*, 552–556.
31. Matsumoto, M. Spread Monolayers of a Water-Soluble Protein (Ferritin) and Its Two- and Three-Dimensional Arrays. *Langmuir* **1994**, *10*, 3922–3925.
32. Seo, H.-S.; Kim, S.-E.; Park, J.-S.; Lee, J.-H.; Yang, K.-Y.; Lee, H.; Lee, K. E.; Han, S.-S.; Lee, J. A Three-Dimensional Nanostructured Array of Protein Nanoparticles. *Adv. Funct. Mater.* **2010**, *20*, 4055–4061.
33. Kasyutich, O.; Sarua, A.; Schwarzacher, W. Bioengineered Magnetic Crystals. *J. Phys. D: Appl. Phys.* **2008**, *41*, 134022.
34. Kasyutich, O.; Tatchev, D.; Hoell, A.; Ogrin, F.; Dewhurst, C.; Schwarzacher, W. Small Angle X-ray and Neutron Scattering Study of Disordered and Three Dimensional-Ordered Magnetic Protein Arrays. *J. Appl. Phys.* **2009**, *105*, 07B528.
35. Meldrum, F.; Heywood, B.; Mann, S. Magnetoferritin: *In Vitro* Synthesis of a Novel Magnetic Protein. *Science* **1992**, *257*, 522–523.
36. Gider, S.; Awschalom, D.; Douglas, T.; Mann, S.; Chaparala, M. Classical and Quantum Magnetic Phenomena in Natural and Artificial Ferritin Proteins. *Science* **1995**, *268*, 77–80.
37. Luis, F.; Petroff, F.; Torres, J. M.; García, L. M.; Bartolomé, J.; Carrey, J.; Vaurès, A. Magnetic Relaxation of Interacting Co Clusters: Crossover from Two- to Three-Dimensional Lattices. *Phys. Rev. Lett.* **2002**, *88*, 217205.
38. Farrell, D.; Ding, Y.; Majetich, S. A.; Sanchez-Hanke, C.; Kao, C.-C. Structural Ordering Effects in Fe Nanoparticle Two- and Three-Dimensional Arrays. *J. Appl. Phys.* **2004**, *95*, 6636–6638.
39. Kasyutich, O.; Desautels, R. D.; Southern, B. W.; van Lierop, J. Novel Aspects of Magnetic Interactions in a Macroscopic 3d Nanoparticle-Based Crystal. *Phys. Rev. Lett.* **2010**, *104*, 127205.
40. Giersig, M.; Hilgendorff, M. Magnetic Nanoparticle Superstructures. *Eur. J. Inorg. Chem.* **2005**, *2005*, 3571–3583.

41. Ge, J.; Hu, Y.; Yin, Y. Highly Tunable Superparamagnetic Colloidal Photonic Crystals. *Angew. Chem., Int. Ed.* **2007**, *46*, 7428–7431.
42. Gupta, A. K.; Gupta, M. Synthesis and Surface Engineering of Iron Oxide Nanoparticles for Biomedical Applications. *Biomaterials* **2005**, *26*, 3995–4021.
43. Kostiainen, M. A.; Kasyutich, O.; Cornelissen, J. J. L. M.; Nolte, R. J. M. Self-Assembly and Optically Triggered Disassembly of Hierarchical Dendron–Virus Complexes. *Nat. Chem.* **2010**, *2*, 394–399.
44. Parker, M. J.; Allen, M. A.; Ramsay, B.; Klem, M. T.; Young, M.; Douglas, T. Expanding the Temperature Range of Biomimetic Synthesis Using a Ferritin from the Hyperthermophile *Pyrococcus furiosus*. *Chem. Mater.* **2008**, *20*, 1541–1547.
45. Tatur, J.; Hagedoorn, P.-L.; Overeijnder, M.; Hagen, W. A Highly Thermostable Ferritin from the Hyperthermophilic Archaeal Anaerobe *Pyrococcus Furiosus*. *Extremophiles* **2006**, *10*, 139–148.
46. Smet, M.; Liao, L.-X.; Dehaen, W.; McGrath, D. V. Photolabile Dendrimers Using *o*-Nitrobenzyl Ether Linkages. *Org. Lett.* **2000**, *2*, 511–513.
47. Il'ichev, Y. V.; Schwörer, M. A.; Wirz, J. Photochemical Reaction Mechanisms of 2-Nitrobenzyl Compounds: Methyl Ethers and Caged ATP. *J. Am. Chem. Soc.* **2004**, *126*, 4581–4595.
48. Wong, W. K.; Schupp, H.; Schnabel, W. Kinetic-Mechanistic Studies on the Photorearrangement of *o*-Nitrobenzyl Ester Groups in Polymer Matrices. *Macromolecules* **1989**, *22*, 2176–2181.
49. Bordi, F.; Cametti, C.; Marianecci, C.; Sennato, S. Equilibrium Particle Aggregates in Attractive Colloidal Suspensions. *J. Phys.: Condens. Matter* **2005**, *17*, S3423.
50. Foffi, G.; McCullagh, G. D.; Lawlor, A.; Zaccarelli, E.; Dawson, K. A.; Sciortino, F.; Tartaglia, P.; Pini, D.; Stell, G. Phase Equilibria and Glass Transition in Colloidal Systems with Short-Ranged Attractive Interactions: Application to Protein Crystallization. *Phys. Rev. E* **2002**, *65*, 031407.
51. Velev, O. D. Self-Assembly of Unusual Nanoparticle Crystals. *Science* **2006**, *312*, 376–377.
52. Doni, G.; Kostiainen, M. A.; Danani, A.; Pavan, G. M. Generation-Dependent Molecular Recognition Controls Self-Assembly in Supramolecular Dendron–Virus Complexes. *Nano Lett.* **2011**, *11*, 723–728.
53. Häussler, W.; Wilk, A.; Gapinski, J.; Patkowski, A. Interparticle Correlations Due to Electrostatic Interactions: A Small Angle X-ray and Dynamic Light Scattering Study. I. Apoferritin. *J. Chem. Phys.* **2002**, *117*, 413–426.
54. Leblanc, M. D.; Plumer, M. L.; Whitehead, J. P.; Mercer, J. I. Transition Temperature and Magnetic Properties of the Granular Ising Model in Two Dimensions Studied by Monte Carlo Simulations: Impact of Intragrain Spin Structure. *Phys. Rev. B* **2010**, *82*, 174435.
55. Plumer, M. L.; van Lierop, J.; Southern, B. W.; Whitehead, J. P. Micromagnetic Simulations of Interacting Dipoles on an fcc Lattice: Application to Nanoparticle Assemblies. *J. Phys.: Condens. Matter* **2010**, *22*, 296007.
56. Shendruk, T. N.; Desautels, R. D.; Southern, B. W.; van Lierop, J. The Effect of Surface Spin Disorder on the Magnetism of γ-Fe_2O_3 Nanoparticle Dispersions. *Nanotechnology* **2007**, *18*, 455704.
57. Aquino, R.; Depeyrot, J.; Sousa, M. H.; Tourinho, F. A.; Dubois, E.; Perzynski, R. Magnetization Temperature Dependence and Freezing of Surface Spins in Magnetic Fluids Based on Ferrite Nanoparticles. *Phys. Rev. B* **2005**, *72*, 184435.
58. Kasyutich, O.; Ilari, A.; Fiorillo, A.; Tatchev, D.; Hoell, A.; Ceci, P. Silver Ion Incorporation and Nanoparticle Formation inside the Cavity of *Pyrococcus furiosus* Ferritin: Structural and Size-Distribution Analyses. *J. Am. Chem. Soc.* **2010**, *132*, 3621–3627.
59. Kostiainen, M. A.; Smith, D. K.; Ikkala, O. Optically Triggered Release of DNA from Multivalent Dendrons by Degrading and Charge-Switching Multivalency. *Angew. Chem., Int. Ed.* **2007**, *46*, 7600–7604.